

Site-Specific Ligand Interactions Favor the Tetragonal Distortion of PbS Nanocrystal Superlattices

Jiří Novák,^{¶,†,‡} Rupak Banerjee,^{¶,§} Andreas Kornowski,^{||} Maciej Jankowski,[⊥] Alexander André,[#] Horst Weller,^{||} Frank Schreiber,^{▽,◆} and Marcus Scheele^{*,#,◆}

[†]Central European Institute of Technology, Masaryk University, Kamenice 5, CZ-62500 Brno, Czech Republic

[‡]Department of Condensed Matter Physics, Masaryk University, Kotlářská 2, CZ-61137 Brno, Czech Republic

[§]Department of Physics, Indian Institute of Technology Gandhinagar, Palaj, Gandhinagar 382355, India

^{||}Institute of Physical Chemistry and The Hamburg Centre for Ultrafast Imaging, University of Hamburg, Grindelallee 117, 20146 Hamburg, Germany

[⊥]Beamline ID03, European Synchrotron Radiation Facility, Grenoble F-38043, France

[#]Institute of Physical and Theoretical Chemistry, University of Tübingen, Auf der Morgenstelle 18, 72076 Tübingen, Germany

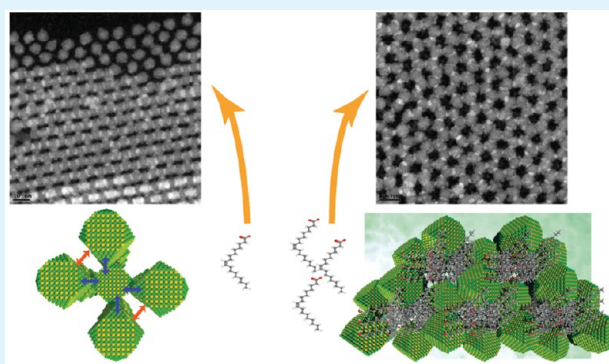
[▽]Institute of Applied Physics, University of Tübingen, Auf der Morgenstelle 10, 72076 Tübingen, Germany

[◆]Center for Light–Matter Interaction, Sensors & Analytics, University of Tübingen, Auf der Morgenstelle 15, 72076 Tübingen, Germany

Supporting Information

ABSTRACT: We analyze the structure and morphology of mesocrystalline, body-centered tetragonal (bct) superlattices of PbS nanocrystals functionalized with oleic acid. On the basis of combined scattering and real space imaging, we derive a three-dimensional (3D) model of the superlattice and show that the bct structure benefits from a balanced combination of $\{100\}_{\text{PbS}}-\{100\}_{\text{PbS}}$ and $\{111\}_{\text{PbS}}-\{111\}_{\text{PbS}}$ interactions between neighboring layers of nanocrystals, which uniquely stabilizes this structure. These interactions are enabled by the coaxial alignment of the atomic lattices of PbS with the superlattice. In addition, we find that this preferential orientation is already weakly present within isolated monolayers. By adding excess oleic acid to the nanocrystal solution, tetragonal distortion is suppressed, and we observe assembly into a bilayered hexagonal lattice reminiscent of a honeycomb with grain sizes of several micrometers.

KEYWORDS: nanocrystals, self-assembly, X-ray scattering, electron microscopy, mesocrystals



INTRODUCTION

Bottom-up engineering of nanocrystal (NC) superlattices with novel electronic properties requires deep insights into the fundamental processes guiding the NCs into a preferred superlattice phase. Of particular importance is the question whether NCs assemble randomly with respect to their atomic planes or along a certain direction of the atomic lattice, and what facilitates such iso-oriented attachment.^{1–4} Superlattices consisting of iso-oriented, single-crystalline NCs are referred to as “mesocrystals”,^{5–7} which are highly sought-after candidates for application as photonic crystals, as magnetic storage media, and in technical devices where large stiffness in combination with high elasticity is desired.^{8–10} It is expected that the electronic properties of mesocrystals will change dramatically depending on how the atomic lattices are oriented with respect to the NC lattice.¹¹ This is especially relevant in light of recent attempts to synthesize conductive mesocrystals with the

potential to experimentally exploit these (so far) theoretical predictions.¹²

For NC ensembles with a sufficiently narrow size distribution, one often observes a close-packed sphere-type assembly into superlattices, which resembles the preferred assembly of metal atoms into body-centered cubic (bcc) or face-centered cubic (fcc) structures.^{13–15} However, recent studies have demonstrated that superlattices with a reduced symmetry following a tetragonal distortion along the Bain path are also frequently observed.^{1,4,16–18} Such body-centered tetragonal (bct) superlattices resemble the packing of iron atoms in steel (martensite phase) and pose an intermediate between the two highly symmetric extremes of bcc and fcc structures. Every rational design of a mesocrystalline super-

Received: June 10, 2016

Accepted: August 9, 2016

Published: August 9, 2016

lattice of NCs with tuned electronic properties will benefit greatly from an improved understanding of the origin of this distortion, which despite recent time-resolved X-ray scattering studies continues to pose many open questions.¹⁸

Recently, Boneschancher et al.² reported on a new mesocrystalline phase of PbSe NCs, which resembles a honeycomb NC superlattice. Such honeycomb superlattices are an excellent example of how controlled self-assembly of a seemingly simple system like rock-salt PbSe NCs can lead to entirely new, rather complex superlattices. Honeycomb superlattices of CdSe (which are easily obtained from PbSe superlattices via cation exchange) bear the potential to be “graphene-like” since their electronic structure is expected to contain Dirac cones, which gives rise to advanced electronic applications such as topological insulators.^{19,20} However, insights into the formation mechanism of the honeycomb phase remain limited.

In this article, we show that the bct phase benefits from a unique combination of ligand interactions between specific NC facets, suggesting an explanation why this phase is often favored over cubic structures in PbS NC superstructures. While these interactions can be tracked to a significant degree already within the first monolayer, they become very pronounced upon adding the second monolayer. The addition of excess oleic acid disrupts these site-specific interactions and leads to disappearance of the bct phase. Instead, we observe the occurrence of a honeycomblike, bilayered hexagonal lattice that lacks any orientational order of atomic lattices.

RESULTS

PbS NCs capped with oleic acid/ Cl^- , cuboctahedral NC shape, and a first excitonic transition maximum at 0.76 eV are prepared following Weidman et al.²¹ We use established sizing curves from literature to derive the effective particle diameter via the energy of the first excitonic transition maximum, which gives 6.3 nm.²² The NCs appear to be partially covered with amorphous clusters of a material with high Z-contrast (Figure S1). We hypothesize that these clusters consist of a lead species, presumably lead oleate, and note a recent study on the role of lead oleate nanoparticles during the early stages of lead chalcogenide NC synthesis under similar conditions.²³ For a sample prepared according to the established method of Shevchenko et al.²⁴ (evaporation-induced self-assembly from a tilted substrate) at an NC concentration of 0.5 mg/mL, we obtain the two-dimensional (2D) grazing incidence small-angle X-ray scattering (GISAXS) pattern displayed in Figure 1.

We find that a typical diffraction pattern is best fit to a bct structure with $a = b = 10.7$ nm and $c = 12.8$ nm, confirming previous observations that superlattices of oleic acid functionalized PbS NCs are often tetragonally distorted.^{1,4} (From here on, we will denote all crystallographic attributions of the NC superlattices with an SL subscript and those attributed to the PbS atomic lattice with a PbS subscript.) The pattern can be attributed to NC crystallites oriented with the $[011]_{\text{SL}}$ and $[001]_{\text{SL}}$ zone axes, respectively, parallel to the sample surface normal. Additionally, we observe a series of weaker powder rings, pointing out that some parts of the NC SLs are randomly oriented with respect to the surface normal, however, with the same lattice constants.³⁷ From the width of the Bragg reflections along the q_z direction and the Scherrer formula, we can estimate the average thickness of the superlattices to be 80 nm, that is, 6–7 unit cells thick.²⁵

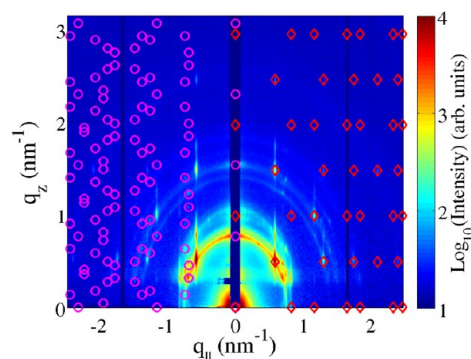


Figure 1. Grazing incidence small-angle X-ray scattering (GISAXS) image measured on NC superlattices (SL). The distinct diffraction spots are simulated according to the NC body-centered tetragonal superlattice oriented with the $[011]_{\text{SL}}$ (magenta circular markers, left-hand side) and $[001]_{\text{SL}}$ (red rhomboidal markers, right-hand side) zone axes parallel to surface normal, respectively.

While X-ray scattering is a powerful technique to verify the long-range order of such NC assemblies and to obtain a meaningful statistical distribution of the ordering and crystallinity of such NCs, electron microscopy is most successful in probing structural features on a local scale. This is demonstrated for the same NCs assembled under similar conditions on an amorphous carbon film in Figure 2a by use of a high-angle annular dark-field detector in scanning transmission electron microscopy mode (HAADF-STEM). The first monolayer (red circles, Figure 2a, inset) resembles a bcc- $[011]_{\text{SL}}$ surface, but the second monolayer (green circles) attaches in a hybrid fashion that is neither entirely bcc- nor fcc-like. Periodic rod-shaped voids remain in the structure if precisely two monolayers are assembled on top of each other (black spaces in the upper third of Figure 2a), forming a centered-rectangular 2D direct lattice. When a third monolayer is assembled (cyan circles, Figure 2a, inset), it does so by occupying sites slightly shifted from those of the first monolayer. Thus, the pattern deviates from pure bcc- $[011]_{\text{SL}}$ packing. This assembly splits the rod-shaped voids observed for the bilayer in the middle, leaving behind a periodic pattern of almost spherical voids (center of Figure 2a) in a simple rectangular 2D direct lattice. (For an illustrative example of 1–7 monolayers, see Figure S2.) Such a packing principle confirms the body-centered tetragonal (bct) structure, which in this case occurs almost exclusively with the $[011]_{\text{SL}}$ zone axis oriented along the surface normal. As apparent from selected-area electron diffraction (SAED, Figure 2b), the assembly is highly directional with the atomic lattices of all NCs aligned with the $[011]_{\text{PbS}}$ zone axis.

Since the dominant $[011]_{\text{SL}}$ orientation found in transmission electron microscopy (TEM) is somewhat in contradiction to the mixed $[011]_{\text{SL}}$ and $[001]_{\text{SL}}$ orientation derived from GISAXS (Figure 1), we note that our X-ray data show diffraction images statistically averaged over a much larger sample area compared to TEM, amounting to approximately $8500 \mu\text{m} \times 30 \mu\text{m}$. The large area necessarily also contains thicker NC grains (of many unit cells), while TEM measurements are mostly constricted to parts of the sample with thicknesses of a few monolayers. We conclude that, for thin superlattices, there is a strong preference for $[011]_{\text{SL}}$ and $[011]_{\text{PbS}}$ orientations relative to the surface normal of NC grains and atomic lattices, respectively, which becomes

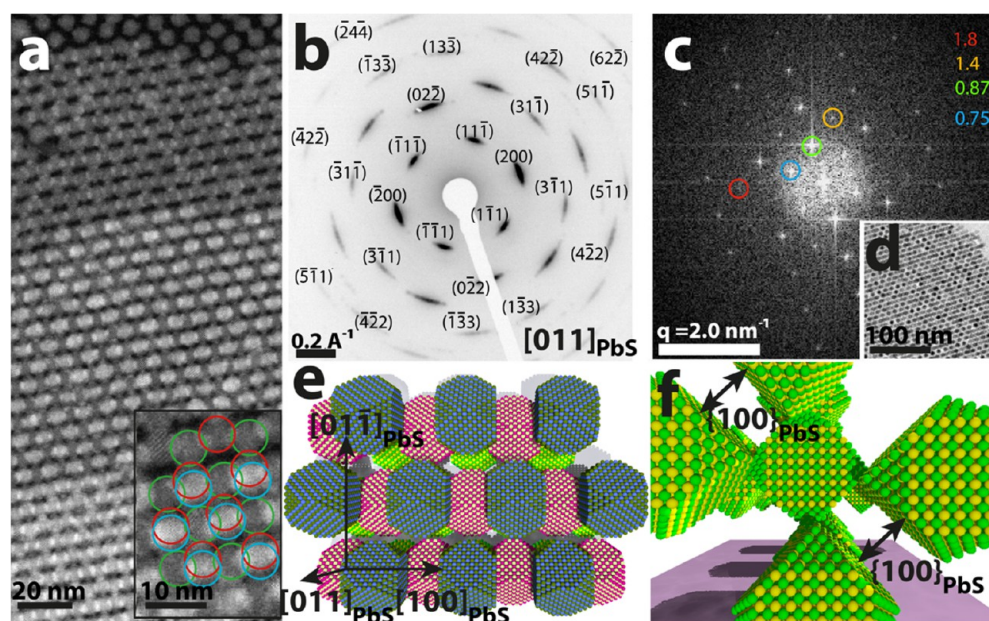


Figure 2. Directional assembly into bct superlattices. (a) HAADF-STEM micrograph of a mesocrystal in the bct phase. From top to bottom, the thickness of the superlattice increases from 1 to 4 layers. (Inset) Packing principle for three consecutive monolayers of NCs marked by red, green, and cyan circles. (b) SAED pattern of 2–3 monolayers indexed according to the $[011]_{\text{PbS}}$ zone axis. All diffraction spots originate from atomic periodicities. (c) Fast Fourier transform (FFT) of the bright-field image of the selected area (d) from which diffraction is recorded. All values are in q space in units of nm^{-1} . (e) Top view of an idealized schematic of a trilayered mesocrystal in the bct phase. Surface ligands are omitted for clarity, and NCs in each layer are displayed in the same color. The crystallographic directions of the PbS lattices are displayed. (f) Side view of the same illustration. The labeled $\{100\}_{\text{PbS}}$ facets of the PbS atomic lattice are directly facing each other.

weakened as the thickness of the superlattice increases. Such preferred orientation is in line with recent observations by Weidman et al.¹⁸ as well as with additional X-ray reflectivity data we have taken of a similar but significantly thinner NC superlattice sample assembled from the same set of NCs (Figure S3).

The evolution of voids in the bct phase is also tracked by fast Fourier transform (FFT, Figure 2c) of a region with 2–3 monolayers (real-space image in Figure 2d). The reciprocal lattice is mostly simple rectangular, with lattice parameters $a = 7.2$ nm and $b = 5.2$ nm, but additional periodicities (namely, at $q = 0.75, 1.4,$ and 1.8 nm^{-1}) are also observed. These periodicities originate from regions with only two layers, representing the centered-rectangular lattice with otherwise identical lattice parameters. Analyzing the lattice of voids also helps in understanding the superstructure of the assembled NCs, as it should contain the same periodicities. All the direct 2D lattices of NCs displayed in Figure 2 can be seen as $[011]_{\text{SL}}$ orientations of a body-centered structure with $a = 10.4$ nm. Upon comparing the SAED, FFT and corresponding superlattice reconstruction in Figure 2 b,c,e, it follows that the $\{100\}_{\text{PbS}}$ planes are parallel to the $\{100\}_{\text{SL}}$ planes of the bct-NC superlattice.

Overall, this real-space analysis is in good agreement with the structural data extracted by X-ray scattering in that (1) we find qualitative evidence for a tetragonal distortion, (2) the cell parameter for the basal plane ($a = 10.4$ nm) is in good agreement with the parameter extracted by GISAXS fitting ($a = 10.7$ nm), and (3) the preferred orientation normal to the substrate is $[011]_{\text{SL}}$. We note that slight differences in self-assembly conditions of oleic acid functionalized PbS NCs (such as drying time, solvent vapor pressure above the surface, nature of the substrate, etc.) are well-known to change the lattice constant of the resulting superstructures by several angstroms,

even if the NC sample, solvent utilized, and concentrations are identical.^{1,4,26} In addition, and on the basis of limited resolution, we estimate the measurement inaccuracy for lattice parameters extracted from the FFT images to be on the order of ~ 1 Å.

Figure 2e displays a schematic top view of a trilayer of PbS NCs in the bct phase, taking into account all the experimental data from above. It is evident that, upon assembly of two layers on top of each other, the $\{111\}_{\text{PbS}}$ facets of the NCs in both layers come in very close contact. Since this interaction would be maximized for pure bcc- $[110]_{\text{SL}}$ packing, we suspect an additional interaction between the surface ligands of NCs of adjacent monolayers to be operative. A possible explanation is given in Figure 2f, which is a side view perpendicular to that in Figure 2e. In the bct phase, a favorable interaction between the surface ligands of $\{100\}_{\text{PbS}}$ facets of NCs diagonally opposite to each other emerges.

Previous studies have revealed the pivotal role of ligand shell thickness on the crystal structure of PbS superlattices obtained from evaporation-induced self-assembly.²⁷ For increasing thickness, the resulting lattice is expected to change from mesocrystalline bcc to mesocrystalline fcc and finally nondirectional bcc. We expand these studies by investigating the effect of a large excess of ligand on assembly of PbS NCs: we add 0.3 mol/L oleic acid to the solution of PbS NC in hexanes. On the assumption of roughly spherical NCs, this corresponds to an excess of 4×10^6 oleic acid molecules/NC. A substrate (either Si or carbon-coated Cu grids) is mounted in the upper part at the bottom of a tilted vial to ensure that oleic acid is present during NC assembly but does not dry on the substrate itself. Although the results reported are also largely observed upon just adding oleic acid, we find it beneficial to simultaneously lower the NC concentration to 0.05 mg/mL. Under these conditions, we observe assembly into a bilayered hexagonal

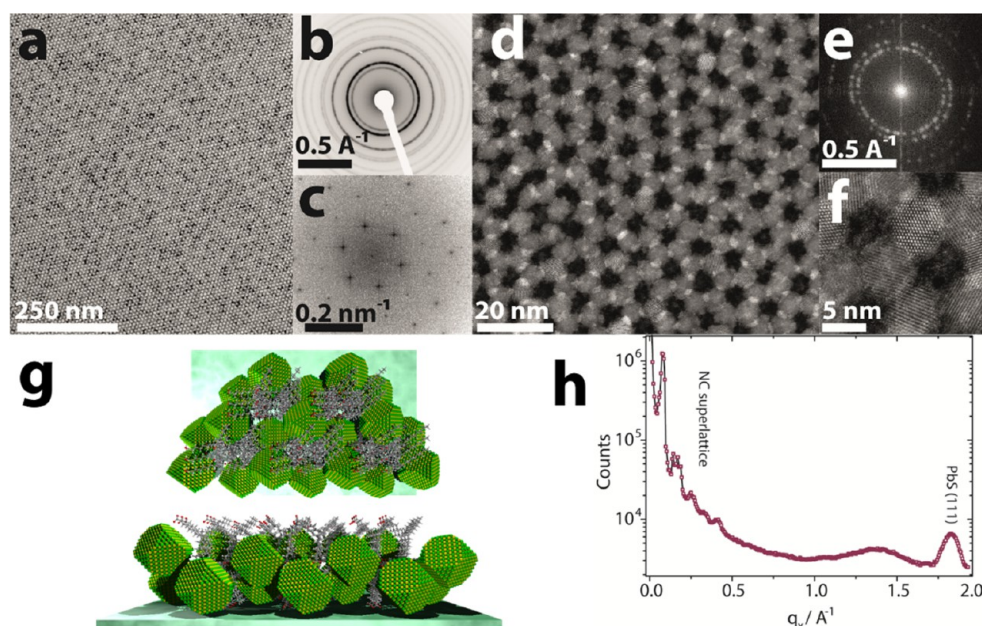


Figure 3. Nondirectional assembly into bilayered hexagonal superlattices. (a) TEM micrograph, (b) $\sim 1 \mu\text{m}^2$ SAED, and (c) FFT of a typical lattice. (d) HAADF-STEM micrograph of a hexagonal bilayer, where NCs are white and the background appears in black, and (e) corresponding FFT. The random orientation of lattice planes indicates nondirectional assembly. (f) High-resolution HAADF-STEM micrograph to illustrate the random orientation of individual NCs. (g) Idealized schematic of a hexagonal bilayer in top and side view with nanoclusters of free oleic acid inside the honeycomb-like voids. NC-bound oleic acid molecules are omitted for clarity. (h) GIXD of macroscopic sample area of a PbS NC superlattice assembled under conditions favoring the bilayered hexagonal superlattice phase. The broad feature around $q = 1.4 \text{ \AA}^{-1}$ may be related to oleic acid.

lattice with domain sizes on the micrometer scale as demonstrated in Figure 3 and Figure S4. While the similarities of the superlattice to a recent work on assembly of PbSe NCs by Boneschanscher et al.² are obvious, we note an important difference. In the present work, the assembly is entirely nondirectional, leading to a random orientation of the individual NC atomic lattices as apparent from SAED (Figure 3b). This kind of lattice has recently been demonstrated by Cargnello et al.²⁸ for PbSe NCs assembled under different conditions at the liquid/air interface. The FFT (Figure 3c) of the bright-field TEM image (Figure 3a) reveals the periodicities in the film, which can be described as hexagonally close-packed voids with a hole-to-hole distance of 9.6 nm. With HAADF-STEM imaging (Figure 3d,f), we deduce the building principle of the lattice, which is similar to that reported in ref 28: two hexagonally close-packed monolayers of NCs are stacked on top of each other such that each NC has three close neighbors in the other monolayer. The nondirectional assembly of the NCs is again visible in the FFT (Figure 3e) and the corresponding HAADF-STEM image at higher magnification (Figure 3f) in terms of a random orientation of atomic lattice planes. On the basis of these observations, we hypothesize the microstructure depicted in the idealized schematic in Figure 3g. We suggest that nanoclusters of excess oleic acid reside at the center of the honeycomb voids. This view is supported by the following facts: (1) Oleic acid is well-known to form nanoscale islands upon slow deposition onto a wide range of different substrates.²⁹ In the presence of NCs, such islands could act as templates for formation of the honeycomb NC lattice, which would restrict the growth of oleic acid clusters to the size of a honeycomb void. (2) Such hypothetical nanoclusters of oleic acid are expected to show a broad scattering signal around 1.4 \AA^{-1} , corresponding to the average distance ($\sim 4.5 \text{ \AA}$) of neighboring oleic acid molecules, which are typically found

upright standing on substrates even in the liquid phase.³⁰ We indeed find a broad feature centered about 1.38 \AA^{-1} (full width at half-maximum $\sim 0.34 \text{ \AA}^{-1}$) in grazing incidence X-ray diffraction (GIXD, Figure 3h) in line with the expected value for *cis*-9-octadecenoic acid (oleic acid) at 298 K.³⁰ This feature is quite specific, first due to its width, which is larger than for the diffraction peaks originating from both the NC superlattice and the 111 reflection of the PbS lattice. The peak width, which is indirectly proportional to the crystal grain size, indicates that the feature originates from an object which is much smaller or at least much less ordered than the PbS NCs. Second, the peak position around 1.38 \AA^{-1} is, on the one hand, far above the q_x range where the SL diffraction peaks are observed (i.e., below 0.5 \AA^{-1}), and on the other hand it is below the position of the first allowed reflection of the PbS fcc lattice (111 reflection at $q_{\text{PbS},111} = 1.83 \text{ \AA}^{-1}$). (3) The presence of oleic acid nanoclusters could potentially explain the nonoriented assembly of NCs into the bilayered hexagonal lattice. The nanoclusters would come rather close to the ligand sphere of the surrounding NCs, and intercalation between the two organic layers might inhibit an unhindered oriented attachment of the NCs in the lattice. As an alternative explanation, we note the previously mentioned effect of a thick ligand shell, which can also prevent oriented attachment without the presence of nanoclusters of the free ligand. Under such circumstances, one typically observes assembly into fcc superlattices without a preferred orientation of the atomic lattices.³¹ However, this would not explain the occurrence of the scattering feature at 1.38 \AA^{-1} , which is a clear indication for oleic acid clusters. In addition, the roughly 10^6 -fold excess of free oleic acid molecules per NC should facilitate the formation of such clusters in the present case considerably.

To investigate whether directional assembly into true honeycomb lattices (such as those reported in ref 2) under the conditions specified above is just kinetically hindered, we

heat the same sample in ultrahigh vacuum (UHV) stepwise to 200 °C and record in situ TEM, SAED, and HAADF-STEM images (Figure 4). First structural as well as crystallographic

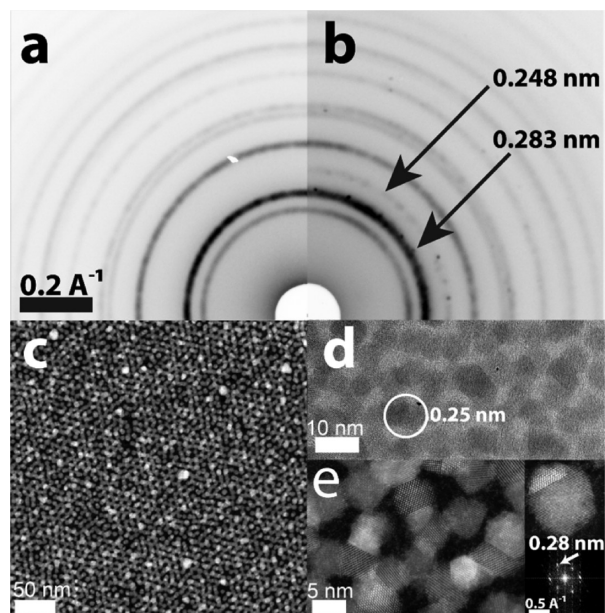


Figure 4. (a, b) Comparison of SAED of the bilayered hexagonal superlattice depicted in Figure 3 (a) vs the same area after in situ heating to 200 °C in ultrahigh vacuum (inside the TEM) (b). Two additional reflections appear at $d = 2.48$ and 2.83 Å, which are not part of the PbS lattice. (c) The bilayered hexagonal superlattice is found to be structurally stable until about 170 °C, but at 200 °C the ordered superlattice is destroyed as shown in STEM image. (d, e) The new lattice fringes are also found on individual quantum dots in HRTEM micrographs (d) and the HAADF-STEM image (including its FFT) (e).

changes become apparent at 170 °C and quickly develop at 200 °C: The superlattice is destroyed (Figure 4c) and the random orientation of atomic lattices prevails. This is consistent with an earlier work by Goodfellow et al.³² on annealing of PbSe superlattices under similar conditions. A comparison of the SAED pattern before heating (Figure 4a) with the pattern after heating (Figure 4b) reveals two new reflections at $d = 0.248$ and 0.283 nm which are both not part of galena (rock-salt PbS). We attribute this new crystallographic phase in the material to elemental lead (relevant d -spacings 0.244/0.281 nm) and emphasize that the necessary reduction of Pb^{2+} to Pb^0 is facilitated by the reducing nature of the electron beam and the UHV conditions as well as the tendency of sulfur to evaporate under such conditions.

In Figure 5 we study the differences between the bct and the bilayered hexagonal phase in more detail. A comparison between a monolayer of NCs in a sample bearing mainly bilayered hexagonal structures (Figure 5a,b) with that in a sample with mainly bct assembly (Figure 5c,d) illustrates that directional assembly of the latter structure is already partially present in the first monolayer: the FFT (Figure 5d) shows a small but significant degree of atomic lattice ordering along the $[011]_{\text{PbS}}$ zone axis. In the analogous FFT of the sample exhibiting a bilayered hexagonal superlattice (Figure 5b), the atomic lattices are randomly distributed.

When a second layer is deposited onto the partially oriented monolayer leading to the bct structure (HR-TEM and corresponding FFT in Figure 5e,f), almost single-crystalline alignment of the atomic lattices of the PbS NCs is observed. This indicates that interlayer interactions, such as those suggested in Figure 2f, are indeed important for the mesocrystalline nature of the bct phase.

DISCUSSION

The results of this work highlight the limitations of the often-cited analogy between atoms and NCs. Because NCs are

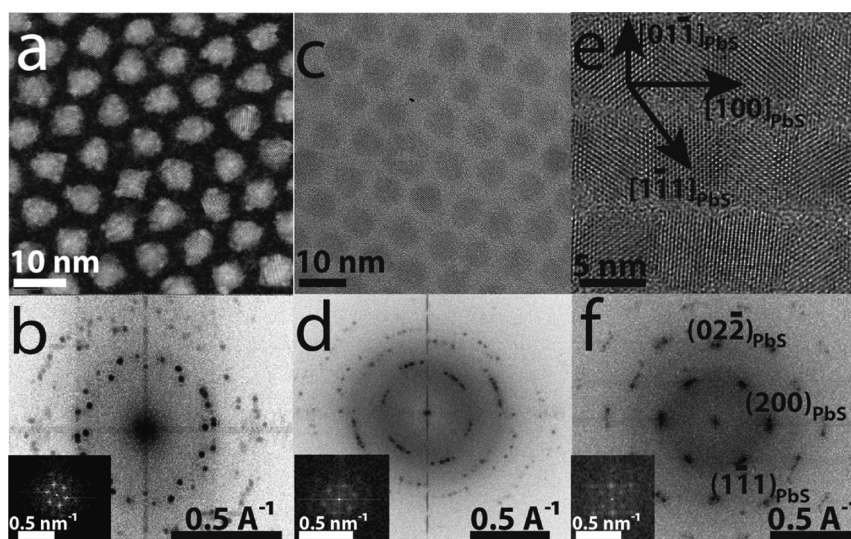


Figure 5. Comparison of the degree of orientation in NC monolayers. (a) HAADF-STEM micrograph of a monolayer in a sample where bilayered hexagonal superlattices are predominant and (b) FFT of the image, displaying the random orientation of atomic lattice planes. (c) TEM micrograph of a monolayer in a sample where the bct phase is predominant and (d) the corresponding FFT. (e) High-resolution TEM micrograph of a bilayered mesocrystal in the bct phase. The displayed crystallographic directions are based on the measured lattice plane spacings. (f) FFT of the image in panel e; indexing is according to the $[011]_{\text{PbS}}$ zone axis. The three insets in panels b, d, and f are magnifications of the center of the corresponding FFT, revealing the periodicities of the evolving superlattice.

faceted and the binding energy of ligands varies considerably for different facets, complex superlattice structures evolve that go far beyond the highly symmetric cubic structures of metals, for instance.³³ Our results suggest the following conclusions:

Preference for $\{111\}_{\text{PbS}}-\{111\}_{\text{PbS}}$ Surface Ligand Interactions. Simon et al.³ have shown that PbS/oleic acid NCs preferably align in the $[011]_{\text{PbS}}$ direction due to fibrillation and favorable $\{111\}_{\text{PbS}}-\{111\}_{\text{PbS}}$ interactions between adjacent NCs within the layer. We find that similar interactions may also be operational between two individual layers on top of each other (Figures 2 and 5). Such interactions would render the NCs a “patchy particle” system and explain the pronounced mesocrystallinity, which is often observed in superlattices of PbS/oleic acid NCs.³⁴ Under the assembly conditions specified in this work, there is a strong preference for the superlattices to grow with the $[011]_{\text{SL}}$ direction normal to the substrate. As illustrated in Figure 2e, this preference is readily explained by $\{111\}_{\text{PbS}}-\{111\}_{\text{PbS}}$ interactions. This is in full accordance with time-resolved X-ray scattering studies of the assembly of PbS superlattices, one of them published during writing of this paper, which showed that alignment of neighboring $\{111\}_{\text{PbS}}$ occurs very early during assembly.^{1,18}

Regarding the nature of such interactions, we suspect that it is mainly van der Waals (vdW) forces between the ligand spheres of neighboring facets, sometimes also referred to as “organic fibrillation”, that are responsible for the attractions.³ This is based on the fact that superlattices are assembled at room temperature and from stable colloidal solutions stored under inert conditions. For such samples, vdW interactions between ligand shells are often seen to dominate.^{1,3,26} For aged samples, oxidation-induced ligand desorption (preferentially from $\{100\}_{\text{PbS}}$ facets) is known to favor direct NC–NC interactions, whereas mild annealing can lead to thin PbS bridges between neighboring NCs.^{3,31} However, these scenarios are less likely in the present case. For very large ligand coverage of the NC surface, the facet specificity of ligand–ligand vdW interactions, that is, the “patchiness” of the NCs, appears to be lost and the bct structure is no longer observed, in accordance with earlier reports.^{18,31} The potential additional role of oleic acid clusters in this respect has already been discussed in the context of Figure 3.

Origin of the Tetragonal Distortion. Bain distortions from pure body-centered ($a = c$) or face-centered ($\sqrt{2}a = c$) cubic packing in superlattices of NCs can have various reasons. Bian et al.¹ as well as Wang et al.⁴ held particle–substrate interactions (e.g., with the walls of a glass vial) during evaporation-induced self-assembly responsible for the occurrence of a bct structure. Concentration gradients during solvent evaporation are known to induce shear forces and residual strain in the assembled superlattices, which can also impact the structure. While we cannot rule out that such effects play a role in our case, too, we emphasize that we repeatedly obtain a bct structure even on different substrates and with or without interactions with the wall of the vial. Therefore, the possible role of ligand–ligand interactions from neighboring $\{100\}_{\text{PbS}}$ facets, as detailed in Figure 2f, should also be considered in order to explain the Bain distortion. We note again the recent study by Weidman et al.,¹⁸ showing that an alignment of $\{100\}$ facets occurs immediately before the Bain distortion is observed. To further illustrate this, we summarize the most important facet–facet interactions and their differences for the fcc, bct, and bcc structures in Figure 6. For a 3D superlattice of PbS NCs with $[011]_{\text{SL}}$ orientation and coaxially oriented

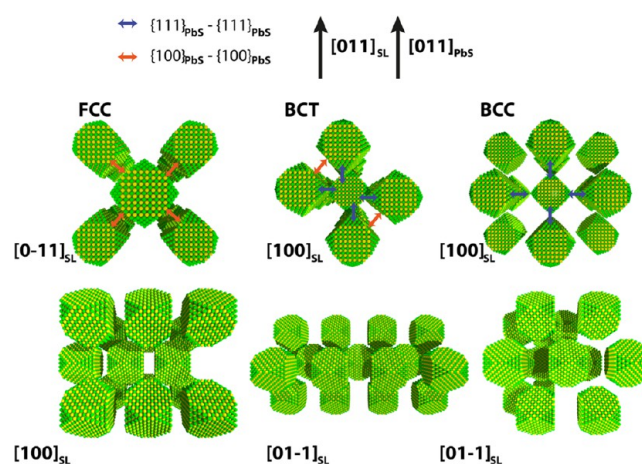


Figure 6. Illustration of predominant ligand–ligand interactions on neighboring facets in cubooctahedral PbS NC superlattices for fcc, bct, and bcc packing. NC superlattices as well as atomic lattices are oriented with the $[011]_{\text{SL}}$ and $[011]_{\text{PbS}}$ axes vertical. Each column of cartoons represents the NC ordering in one of the three packing types. The top row of cartoons represents an in-plane view (i.e., side view with respect to the sample) of PbS mesocrystals with the specified superlattice direction along the view direction. The bottom row of cartoons is obtained by a 90° in-plane rotation of the structures in the top row around the vertical axis. Interactions between ligands on the $\{111\}_{\text{PbS}}$ facets of the NCs are denoted in blue, and interactions of ligands on the $\{100\}_{\text{PbS}}$ facets are marked in red. Ligand spheres are omitted for clarity.

atomic lattices, $\{100\}_{\text{PbS}}$ facets from opposite-above exhibit significant overlap only for fcc or bct packing. In a bcc lattice, the overlap would be zero (e.g., the facets are too far away). On the other hand, notable overlap between $\{111\}_{\text{PbS}}$ facets of different layers is present only in bcc (maximized) or bct packing. Thus, only in the bct structure is a good balance achieved for ligand interactions between $\{100\}_{\text{PbS}}$ and $\{100\}_{\text{PbS}}$ facets and between $\{111\}_{\text{PbS}}$ and $\{111\}_{\text{PbS}}$ facets, which we believe to be an important driving force for the occurrence of tetragonal distortion.

This also follows from a general consideration of the coordination number (CN) in bcc structures and its evolution along the Bain path. In pure bcc packing, the nearest-neighbor distance is the cube diagonal or half the spacing of the $\{111\}_{\text{PbS}}$ planes, resulting in a CN of 8. As a result of a Bain distortion, the CN increases to $8 + 4$ with eight interactions in the $\{111\}_{\text{SL}}$ directions and four interactions in the $\{100\}_{\text{SL}}$ directions, which are next-nearest neighbors. Since the atomic lattices in the present structure are coaxially aligned, this translates into eight $\{111\}_{\text{PbS}}-\{111\}_{\text{PbS}}$ and four $\{100\}_{\text{PbS}}-\{100\}_{\text{PbS}}$ interactions between NC facets within one unit cell. In an fcc structure, the CN is 12 and thus largest, but for coaxial alignment this exclusively involves $\{100\}_{\text{PbS}}-\{100\}_{\text{PbS}}$ and no $\{111\}_{\text{PbS}}-\{111\}_{\text{PbS}}$ interactions. (Note that there are diverging results in literature how fcc-packed superlattices of PbS NCs align atomically: coaxially, partially $111_{\text{SL}} \parallel 110_{\text{PbS}}$, or not at all.^{18,27,31})

For the present bct structure, the nearest-neighbor spacing, given by $\text{NN}_{\text{bct}} = [(2a^2 + 2c^2)^{1/2}]/2$, is 9.9 nm, while the four next-nearest neighbors are $a = 10.7$ nm apart. These distances mark the spacings between adjacent $\{111\}_{\text{PbS}}$ and $\{100\}_{\text{PbS}}$ facets. For a bcc structure with the same nearest-neighbor spacing, the $\{111\}_{\text{PbS}}$ facets would be 9.9 nm apart, and the $\{100\}_{\text{PbS}}$ facets, 11.4 nm apart. This comparison further

illustrates the good balance between the two type of interactions in the bct versus bcc structure.

For completeness, the situation may change for oleic acid-deficient NC surfaces like those utilized by Boneschanscher et al.² Under such conditions, the larger surface energy of the {100} facet of PbS(e) NCs seems to become the dominating factor, and the now partially ligand-depleted NCs are believed to fuse with their {100} facets.^{35,36}

Hindrance of Oriented Attachment in Bilayered Hexagonal Superlattices. Figure 3 demonstrates that it is possible to obtain extended honeycomblike structures of PbS NCs without the need for the Langmuir-type liquid/air assembly procedure utilized in other studies.^{2,28} Different from previous suggestions, oriented attachment is apparently not necessary to favor assembly into this lattice.² While further investigations are necessary to truly understand the driving force for this assembly, the present work suggests that the packing type itself is energetically favorable under certain conditions and that templating effects due to nanoclusters of excess ligand may play a pivotal role. Our in situ heating studies show that oriented attachment in the presence of such oleic acid clusters is strongly hindered and cannot easily be activated by a postassembly annealing step.

CONCLUSION

We describe the microstructure of mesocrystalline, body-centered tetragonal (bct) superlattices of cuboctahedral PbS nanocrystals functionalized with oleic acid. Due to the coaxial alignment of atomic lattices within the superlattice of nanocrystals, the bct structure benefits from a combination of favorable $\{100\}_{\text{PbS}}-\{100\}_{\text{PbS}}$ and $\{111\}_{\text{PbS}}-\{111\}_{\text{PbS}}$ interactions, which we believe to be one of the main driving forces for its formation. Addition of excess oleic acid suppresses this driving force and leads to the formation of a bilayered hexagonal superlattice with randomly oriented atomic lattices. This suggests that oriented attachment is not a prerequisite for the formation of honeycomblike lattices of nanocrystals with rock-salt structure. We discuss an alternative mechanism of formation, which involves the potential templating effect of nanoclusters of excess ligand.

METHODS

Synthesis of PbS. The PbS nanocrystal samples were synthesized by a previously reported method.²¹ The nanocrystals were precipitated by addition of anhydrous ethanol, the suspension was centrifuged for 5 min at 4500 rpm, the supernatant was discarded, and the precipitate was dissolved in anhydrous hexanes. It was washed two more times by adding anhydrous ethanol and one more time with acetone. The nanocrystals are stored in anhydrous hexanes. This procedure typically leads to a surface coverage of ~ 3 ligands/nm².

Self-Assembly. Self-assembly was achieved by slow evaporation of the solvent from the nanocrystal suspension placed on a standard carbon-coated 400-mesh TEM copper grid (bottom of the vial) or a planar Si wafer of 1 cm \times 1 cm as substrate at room temperature. In a typical preparation of a bct lattice, 500 μL of PbS nanocrystal hexane dispersion (0.5 mg/mL) was mixed with 50 μL of toluene in a vial. To obtain bilayered hexagonal superlattices, 0.3 mol/L oleic acid was added to a 0.05 mg/mL nanocrystal solution in 500 μL /50 μL toluene. As briefly described earlier, the substrate was dried in a tilted vial to ensure that no residual oleic acid remained on top of the substrate after the solvent meniscus had fallen below the height level of the substrate during drying of the solvent. Due to the large excess, a substantial amount of oleic acid remained at the bottom of the vial after drying, but not on the substrate itself if it was placed in the upper part of the vial. In both cases, the vial was loosely capped with a wet lid

with hexane and the solvent was allowed to evaporate at room temperature for at least 16 h.

X-ray Scattering. GISAXS and GIXD measurements were performed at the ID03 beamline of the European Synchrotron Radiation Facility (Grenoble, France). For GISAXS, the X-ray beam impinged under a grazing angle of 0.2° on the sample surface and the scattering pattern was detected by a 2D Pilatus 300 K detector with pixel size 172 μm at a distance of 170 cm from the sample. The energy of X-rays is 12.9 keV with a bandwidth of 0.01%. The size of the beam was approximately 30 \times 30 μm^2 and the beam divergence was 25 μrad and 200 μrad , providing scattering vector resolution of $1.6 \times 10^{-4} \text{ \AA}^{-1}$ and $1.3 \times 10^{-3} \text{ \AA}^{-1}$ in the vertical and horizontal directions, respectively. GIXD scans are recorded at the same energy by a MaxiPix detector and an incidence angle of 0.1°, well below the critical angle of total external reflection. The resolution, when beam size and pixel-to-pixel distance were taken into account, was 0.05°, corresponding to 0.0055 \AA^{-1} for the laterally slitted down Maxipix detector (GIXD regime); that is, in-plane resolution of the line scans in the GIXD regime was made via moving the delta arm (i.e., detector horizontal angle arm).

Electron Microscopy. TEM and STEM measurements were carried out on a JEOL JEM 2200 FS (field emission transmission electron microscope, with an in-column energy filter) operating at 200 kV, equipped with two CEOS Cs correctors for TEM and STEM modes (CETCOR, CESCOR), a high-angle annular dark-field (HAADF) detector, and a Gatan 4K UltraScan 1000 camera. The in situ heating experiments were performed on a Gatan single-tilt heating holder (model 628 TA).

ASSOCIATED CONTENT

Supporting Information

The Supporting Information is available free of charge on the ACS Publications website at DOI: 10.1021/acsami.6b06989.

Four figures showing electron micrographs of NCs used in this work, TEM micrograph of PbS NCs with increasing layer thickness, XRR profile of a thin NC sample (few monolayers), and low-magnification TEM micrograph of a typical assembly into a honeycomblike lattice (PDF)

AUTHOR INFORMATION

Corresponding Author

*E-mail marcus.scheele@uni-tuebingen.de.

Author Contributions

[¶]J.N. and R.B. contributed equally to this publication.

Notes

The authors declare no competing financial interest.

ACKNOWLEDGMENTS

Financial support of M.S. has been provided in equal parts by the Institutional Strategy of the University of Tübingen (Deutsche Forschungsgemeinschaft, ZUK 63) and the Baden-Württemberg Stiftung by the elite program for postdocs. J.N. acknowledges financial support from Project CEITEC 2020 (Grant LQ1601, financed by Ministry of Education, Youth and Sports of the Czech Republic). We thank Zheng Liu for his contribution during an early stage of this project and Hans-Joachim Schöpe for fruitful discussions.

REFERENCES

- (1) Bian, K.; Choi, J. J.; Kaushik, A.; Clancy, P.; Smilgies, D.-M.; Hanrath, T. Shape-Anisotropy Driven Symmetry Transformations in Nanocrystal Superlattice Polymorphs. *ACS Nano* **2011**, *5* (4), 2815–2823.

- (2) Boneschanscher, M. P.; Evers, W. H.; Geuchies, J. J.; Altantzis, T.; Goris, B.; Rabouw, F. T.; van Rossum, S. A. P.; van der Zant, H. S. J.; Siebbeles, L. D. A.; Van Tendeloo, G.; Swart, L.; Hilhorst, J.; Petukhov, A. V.; Bals, S.; Vanmaekelbergh, D. Long-Range Orientation and Atomic Attachment of Nanocrystals in 2D Honeycomb Superlattices. *Science* **2014**, *344* (6190), 1377–1380.
- (3) Simon, P.; Bahrig, L.; Baburin, I. A.; Formanek, P.; Röder, F.; Sickmann, J.; Hickey, S. G.; Eychmüller, A.; Lichte, H.; Kniep, R.; Rosseeva, E. Interconnection of Nanoparticles within 2D Superlattices of PbS/Oleic Acid Thin Films. *Adv. Mater.* **2014**, *26* (19), 3042–3049.
- (4) Wang, Z.; Schliehe, C.; Bian, K.; Dale, D.; Bassett, W. A.; Hanrath, T.; Klinke, C.; Weller, H. Correlating Superlattice Polymorphs to Internanoparticle Distance, Packing Density, and Surface Lattice in Assemblies of PbS Nanoparticles. *Nano Lett.* **2013**, *13* (3), 1303–1311.
- (5) Bahrig, L.; Hickey, S. G.; Eychmüller, A. Mesocrystalline Materials and the Involvement of Oriented Attachment - a review. *CrystEngComm* **2014**, *16* (40), 9408–9424.
- (6) Cölfen, H.; Antonietti, M. Mesocrystals: Inorganic Superstructures Made by Highly Parallel Crystallization and Controlled Alignment. *Angew. Chem., Int. Ed.* **2005**, *44* (35), 5576–5591.
- (7) Seto, J.; Ma, Y.; Davis, S. A.; Meldrum, F.; Gourrier, A.; Kim, Y.-Y.; Schilde, U.; Sztucki, M.; Burghammer, M.; Maltsev, S.; Jäger, C.; Cölfen, H. Structure-Property Relationships of a Biological Mesocrystal in the Adult Sea Urchin Spine. *Proc. Natl. Acad. Sci. U. S. A.* **2012**, *109* (10), 3699–3704.
- (8) Natalio, F.; Corrales, T. P.; Panthöfer, M.; Schollmeyer, D.; Lieberwirth, I.; Müller, W. E. G.; Kappl, M.; Butt, H.-J.; Tremel, W. Flexible Minerals: Self-Assembled Calcite Spicules with Extreme Bending Strength. *Science* **2013**, *339* (6125), 1298–1302.
- (9) Petit, C.; Motte, L.; Ngo, A.-T.; Lisiecki, I.; Pileni, M.-P. In *Nanocrystals Forming Mesoscopic Structures*; Wiley-VCH Verlag, 2006; pp 251–278; DOI: 10.1002/3527607587.ch10.
- (10) Podsiadlo, P.; Lee, B.; Prakapenka, V. B.; Krylova, G. V.; Schaller, R. D.; Demortière, A.; Shevchenko, E. V. High-Pressure Structural Stability and Elasticity of Supercrystals Self-Assembled from Nanocrystals. *Nano Lett.* **2011**, *11* (2), 579–588.
- (11) Kaushik, A. P.; Lukose, B.; Clancy, P. The Role of Shape on Electronic Structure and Charge Transport in Faceted PbSe Nanocrystals. *ACS Nano* **2014**, *8* (3), 2302–2317.
- (12) Scheele, M.; Bruetting, W.; Schreiber, F. Coupled Organic-Inorganic Nanostructures. *Phys. Chem. Chem. Phys.* **2015**, *17*, 97–111.
- (13) Korgel, B. A.; Fullam, S.; Connolly, S.; Fitzmaurice, D. Assembly and Self-Organization of Silver Nanocrystal Superlattices: Ordered "Soft Spheres". *J. Phys. Chem. B* **1998**, *102* (43), 8379–8388.
- (14) Murray, C. B.; Kagan, C. R.; Bawendi, M. G. Self-Organization of CdSe Nanocrystallites into Three-Dimensional Quantum Dot Superlattices. *Science* **1995**, *270* (5240), 1335–1338.
- (15) Nagel, M.; Hickey, S. G.; Frömsdorf, A.; Kornowski, A.; Weller, H. Synthesis of Monodisperse PbS Nanoparticles and Their Assembly into Highly Ordered 3D Colloidal Crystals. *Z. Phys. Chem.* **2007**, *221*, 427–437.
- (16) Choi, J. J.; Bian, K.; Baumgardner, W. J.; Smilgies, D.-M.; Hanrath, T. Interface-Induced Nucleation, Orientational Alignment and Symmetry Transformations in Nanocube Superlattices. *Nano Lett.* **2012**, *12* (9), 4791–4798.
- (17) Quan, Z.; Wu, D.; Zhu, J.; Evers, W. H.; Boncella, J. M.; Siebbeles, L. D. A.; Wang, Z.; Navrotsky, A.; Xu, H. Energy Landscape of Self-Assembled Superlattices of PbSe Nanocrystals. *Proc. Natl. Acad. Sci. U. S. A.* **2014**, *111* (25), 9054–9057.
- (18) Weidman, M. C.; Smilgies, D.-M.; Tisdale, W. A. Kinetics of the Self-Assembly of Nanocrystal Superlattices Measured by Real-Time in situ X-ray Scattering. *Nat. Mater.* **2016**, *15*, 775.
- (19) Kalesaki, E.; Delerue, C.; Morais Smith, C.; Beugeling, W.; Allan, G.; Vanmaekelbergh, D. Dirac Cones, Topological Edge States, and Nontrivial Flat Bands in Two-Dimensional Semiconductors with a Honeycomb Nanogeometry. *Phys. Rev. X* **2014**, *4* (1), No. 011010.
- (20) Moore, J. E. The Birth of Topological Insulators. *Nature* **2010**, *464* (7286), 194–198.
- (21) Weidman, M. C.; Beck, M. E.; Hoffman, R. S.; Prins, F.; Tisdale, W. A. Monodisperse, Air-Stable PbS Nanocrystals via Precursor Stoichiometry Control. *ACS Nano* **2014**, *8* (6), 6363–6371.
- (22) Segets, D.; Lucas, J. M.; Klupp Taylor, R. N.; Scheele, M.; Zheng, H.; Alivisatos, A. P.; Peukert, W. Determination of the Quantum Dot Band Gap Dependence on Particle Size from Optical Absorbance and Transmission Electron Microscopy Measurements. *ACS Nano* **2012**, *6* (10), 9021–9032.
- (23) Britt, D. K.; Yoon, Y.; Ercius, P.; Ewers, T. D.; Alivisatos, A. P. Hexameric Octahedral Clusters of PbSe Nanocrystals Grown from Amorphous Lead(II) Carboxylate Nanoparticles. *Chem. Mater.* **2013**, *25* (12), 2544–2548.
- (24) Shevchenko, E. V.; Talapin, D. V.; Rogach, A. L.; Kornowski, A.; Haase, M.; Weller, H. Colloidal Synthesis and Self-Assembly of CoPt3 Nanocrystals. *J. Am. Chem. Soc.* **2002**, *124* (38), 11480–11485.
- (25) Warren, B. E. *X-Ray Diffraction*; Addison-Wesley Publishing Co., 1969; p 251.
- (26) Goodfellow, B. W.; Yu, Y.; Bosoy, C. A.; Smilgies, D.-M.; Korgel, B. A. J. The Role of Ligand Packing Frustration in Body-Centered Cubic (bcc) Superlattices of Colloidal Nanocrystals. *Phys. J. Phys. Chem. Lett.* **2015**, *6* (13), 2406–2412.
- (27) Simon, P.; Rosseeva, E.; Baburin, I. A.; Liebscher, L.; Hickey, S. G.; Cardoso-Gil, R.; Eychmüller, A.; Kniep, R.; Carrillo-Cabrera, W. PbS-Organic Mesocrystals: The Relationship between Nanocrystal Orientation and Superlattice Array. *Angew. Chem., Int. Ed.* **2012**, *51* (43), 10776–10781.
- (28) Cargnello, M.; Johnston-Peck, A. C.; Diroll, B. T.; Wong, E.; Datta, B.; Damodhar, D.; Doan-Nguyen, V. V. T.; Herzing, A. A.; Kagan, C. R.; Murray, C. B. Substitutional Doping in Nanocrystal Superlattices. *Nature* **2015**, *524* (7566), 450–453.
- (29) Garland, E. R.; Rosen, E. P.; Clarke, L. L.; Baer, T. Structure of Submonolayer Oleic Acid Coverages on Inorganic Aerosol Particles: Evidence of Island Formation. *Phys. Chem. Chem. Phys.* **2008**, *10* (21), 3156–3161.
- (30) Iwahashi, M.; Kasahara, Y.; Matsuzawa, H.; Yagi, K.; Nomura, K.; Terauchi, H.; Ozaki, Y.; Suzuki, M. Self-Diffusion, Dynamical Molecular Conformation, and Liquid Structures of n-Saturated and Unsaturated Fatty Acids. *J. Phys. Chem. B* **2000**, *104* (26), 6186–6194.
- (31) Choi, J. J.; Bealing, C. R.; Bian, K.; Hughes, K. J.; Zhang, W.; Smilgies, D.-M.; Hennig, R. G.; Engstrom, J. R.; Hanrath, T. Controlling Nanocrystal Superlattice Symmetry and Shape-Anisotropic Interactions through Variable Ligand Surface Coverage. *J. Am. Chem. Soc.* **2011**, *133* (9), 3131–3138.
- (32) Goodfellow, B. W.; Patel, R. N.; Panthani, M. G.; Smilgies, D.-M.; Korgel, B. A. Melting and Sintering of a Body-Centered Cubic Superlattice of PbSe Nanocrystals Followed by Small Angle X-ray Scattering. *J. Phys. Chem. C* **2011**, *115* (14), 6397–6404.
- (33) Boles, M. A.; Talapin, D. V. Self-Assembly of Tetrahedral CdSe Nanocrystals: Effective "Patchiness" via Anisotropic Steric Interaction. *J. Am. Chem. Soc.* **2014**, *136* (16), 5868–5871.
- (34) Zhang; Glotzer, S. C. Self-Assembly of Patchy Particles. *Nano Lett.* **2004**, *4* (8), 1407–1413.
- (35) Boles, M. A.; Talapin, D. V. Connecting the Dots. *Science* **2014**, *344* (6190), 1340–1341.
- (36) Zhrebetskyy, D.; Scheele, M.; Zhang, Y.; Bronstein, N.; Thompson, C.; Britt, D.; Salmeron, M.; Alivisatos, P.; Wang, L.-W. Hydroxylation of the Surface of PbS Nanocrystals Passivated with Oleic Acid. *Science* **2014**, *344* (6190), 1380–1384.
- (37) The additional four diffraction spots at the truncation rods at $q_{\parallel} = \pm 0.59 \text{ nm}^{-1}$ and weaker Debye rings, not centered around the origin at $q = 0 \text{ nm}^{-1}$ and not covered by the simulated peaks (see markers in Figure 1), correspond to the diffracted waves that were additionally reflected on the NC layer/Si substrate interface. Thus, these diffraction spots and Debye rings are vertically shifted by $\Delta q_z = 0.25 \text{ nm}^{-1}$ with respect to diffraction features of equal Miller indices that are formed by waves not reflected on the interface.